Enhanced photocatalytic hydrogen evolution from organic semiconductor heterojunction nanoparticles

Jan Kosco[1*], Matthew Bidwell[2], Hyojung Cha[2], Tyler Martin[3], Calvyn T. Howells[1], Michael Sachs[2], Dalaver Anjum[1], Sandra Gonzalez Lopez[1], Lingyu Zou[2], Andrew Wadsworth[2], Weimin Zhang[1], Lisheng Zhang[1], James Tellam, Rachid Sougrat[1], Frederic Laquai[1], Dean DeLongchamp[3], James R. Durrant[2], Iain McCulloch[1,2*].

Affiliations

[1]King Abdullah University of Science and Technology (KAUST), KAUST Solar Center (KSC), Physical Sciences and Engineering Division (PSE), Thuwal 23955-6900, Saudi Arabia.

[2]Department of Chemistry and Centre for Plastic Electronics, Imperial College London, Exhibition Road, London SW7 2AZ, UK.

[3]Materials Science and Engineering Division, National Institute of Standards and Technology, 100 Bureau Drive, Gaithersburg, Maryland 20899, USA.

*Correspondence to: iain.mcculloch@kaust.edu.sa, jan.kosco@kaust.edu.sa

Abstract

Photocatalysts formed from a single organic semiconductor typically suffer from inefficient intrinsic charge generation, which leads to low photocatalytic activities. We demonstrate that incorporating a heterojunction between a donor polymer (PTB7-Th) and non-fullerene acceptor (EH-IDTBR) in organic nanoparticles (NP) can result in hydrogen evolution photocatalysts with greatly enhanced photocatalytic activity. Control of the nanomorphology of these NPs was achieved by varying the

stabilizing surfactant employed during NP fabrication, converting it from a core-shell structure to an intermixed donor/acceptor blend, and increasing H_2 evolution by an order of magnitude. The resulting photocatalysts display an unprecedentedly high H_2 evolution rate of over 60,000 $\mu molh^{-1}g^{-1}$ under 350 to 800 nm illumination and external quantum efficiencies over 6% in the region of maximum solar photon flux.

The development of sustainable energy sources is essential to avert impending climate change while sustaining the global population and economic growth.[1] Solar energy is by far the greatest available source of renewable energy, but its transience limits its utility.[2] If solar energy is to provide power on a scale commensurate with or exceeding that currently generated from fossil fuels, it must be stored and supplied to users on demand.[2] Storing solar energy in the chemical bonds of a fuel is therefore highly desirable.[2] H_2 is the simplest such "solar fuel" and can be generated from water via electrolysis, or using semiconductor photocatalysts, which absorb light and convert it to electrical charges that drive surface redox reactions. A "particulate" system in which photocatalysts are directly dispersed in water is projected to be the cheapest way of producing solar H_2.[3] In the simplest case, overall water splitting (OWS) can be achieved by a single photocatalyst that simultaneously oxidises and reduces H_2O into H_2 and O_2. However, the only particulate photocatalysts currently capable of driving OWS are typically based on single component, wide bandgap semiconductors such as TiO_2,[4] $SrTiO_3$,[5] or carbon nitrides (CNx)[6,7], which are almost exclusively active at UV wavelengths that constitute <4 % of the solar spectrum.[8] This fundamentally limits their maximum solar to hydrogen efficiency (ηSTH) below the target of 10 % deemed necessary for commercial viability.[3,8] OWS can also be achieved by two photocatalysts operating in parallel, where the hydrogen evolution reaction (HER) and oxygen evolution reaction (OER) take place on separate semiconductors. This "Z-scheme" system is analogous to natural photosynthesis, and can potentially achieve higher ηSTH by employing semiconductors with narrower bandgaps which can absorb a larger proportion of the

solar spectrum.[9] Stable, low cost and efficient O_2 evolution photocatalysts, such as WO_3[10] and $BiVO_4$,[11] are active up to 470 and 510 nm respectively,[12] but the development of stable, efficient and low cost inorganic H_2 evolution photocatalysts (HEPs) has proved more challenging, particularly for HEPs which exhibit complementary absorptions and high activities above 500 nm.[13–15] This greatly limits the ηSTH of current Z-schemes and has prompted the recent interest in developing visible light active HEPs based on organic semiconductors other than CN_x,[7] whose bandgaps can be tuned to absorb further into the visible spectrum. Conjugated polymers[16,17] and covalent organic frameworks (COFs)[18] have attracted the most attention due to their modular structures which enable their energy levels and physical properties to be precisely controlled. However, the external quantum efficiencies (EQEs) of these novel non-CN_x photocatalysts have been limited by the high exciton binding energies and short exciton diffusion lengths (typically 5-10 nm)[19] of organic semiconductors which cause high rates of exciton recombination in the semiconductor bulk,[20] and hence inefficient generation of charges that can drive redox reactions at the photocatalyst surface. To overcome this limitation, most research has been focused on improving exciton dissociation at the photocatalyst surface by increasing the semiconductor/electrolyte interfacial area via nanoparticle (NP) formation, hydrophilicity enhancements and/or by sensitising the photocatalyst surface with a suitable dye to create a donor/acceptor (D/A) semiconductor heterojunction that is able to dissociate excitons at the external photocatalyst/dye interface.[21,22] Less attention has been given to developing organic non-CN_x HEPs with internal semiconductor heterojunctions that can drive exciton dissociation and spatially separate charges in the photocatalyst bulk.[17,23] Conjugated polymer NPs can be readily fabricated with an internal D/A heterojunction by blending donor and acceptor semiconductors together within the same NP.[24] However, this feature has not yet been fully exploited, with most studies to date focusing on optimising the photocatalytic performance of HEP NPs formed of a single conjugated polymer.[25–27]

This work details the development of novel organic semiconductor NP HEPs which incorporate an internal D/A heterojunction that enhances exciton dissociation in the NP bulk, leading to greatly

enhanced photocatalytic activity, compared to single component NPs. By selecting an appropriate stabilizing surfactant employed during NP fabrication, it was possible to optimize the heterojunction morphology from the common, but unfavourable, core-shell structure to a more intimately mixed blend, where both donor and acceptor components are present at the NP surface. This dramatically improved charge extraction from the NPs and resulted in stable (35 h) H_2 evolution photocatalysts with unprecedentedly high activity under broadband visible light illumination, and EQEs exceeding 5% at 660 to 700 nm. These are the highest EQEs at wavelengths > 500 nm reported for any organic HEP to date, and may provide a pathway to high efficiency solar to chemical energy conversion by substantially improving the ηSTH of current Z-schemes.

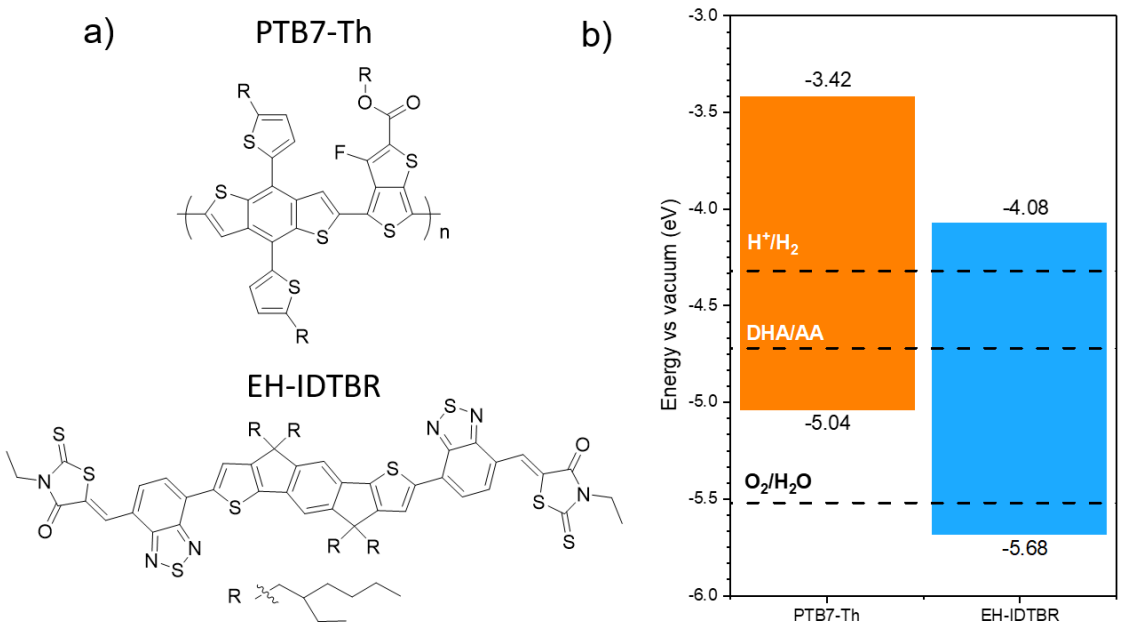

Fig. 1: Materials and energy levels. **a)** Chemical structures of PTB7-Th and EH-IDTBR. **b)** Highest occupied and lowest unoccupied molecular orbital energy levels of PTB7-Th and EH-IDTBR compared to the proton reduction potential (H^+/H_2), water oxidation potential (O_2/H_2O), and the calculated potential of the two hole oxidation of ascorbic acid to dehydroascorbic acid in solution (DHA/AA)[21] at

pH 2 (the experimentally measured pH of 0.2 mol/L ascorbic acid). All energy levels and electrochemical potentials are expressed on the absolute electrochemical scale (0 V vs. SHE = -4.44 V vs Vac.).[28]

NPs were fabricated via the miniemulsion process,[29] initially employing sodium dodecyl sulfate (SDS) as the stabilising surfactant, from the donor polymer Poly([2,6'-4,8-di(5-ethylhexylthienyl)benzo[1,2-b;3,3-b]dithiophene]{3-fluoro-2[(2-ethylhexyl)carbonyl]thieno[3,4-b]thiophenediyl}) (PTB7-Th) matched with the nonfullerene acceptor EH-IDTBR. The NP size distributions were measured by dynamic light scattering (**Fig. S1, Table S1**). This D/A combination was chosen for its strong visible light absorption (**Fig. S2**), type II energy level offset (**Fig. 1**), and interfacial morphology that drives efficient charge separation at the PTB7-Th/EH-IDTBR heterojunction[30] while also generating sufficiently reducing photoexcited electrons in the EH-IDTBR lowest unoccupied molecular orbital (LUMO) to drive the HER with the aid of a Pt co-catalyst as well as sufficiently oxidising holes in the PTB7-Th highest occupied molecular orbital (HOMO) to oxidise ascorbic acid. Pt was photodeposited in-situ on the organic NP surface during all H_2 evolution measurements. Measuring the HER rates of NPs composed of a range of PTB7-Th:EH-IDTBR mass ratios formed using SDS (**Fig. 2a-b**) revealed that all D/A NPs formed from a PTB7-Th:EH-IDTBR blend were significantly more active than single component NPs formed of either pristine PTB7-Th, pristine EH-IDTBR, or both pristine NPs mixed together. The HER rate increase is therefore attributed to enhanced charge generation in the blend NPs driven by their internal D/A heterojunction. This is confirmed by photoluminescence quenching yield (PLQY) measurements, which show partial quenching of both PTB7-Th and EH-IDTBR excitons for all two component NP blend compositions (**Fig. S3**). Interestingly, the maximum HER rate (3044 ± 332 $\mu molh^{-1}g^{-1}$) occurred at a blend ratio (EH-IDTBR mass fraction of 90 %) where there is insufficient PTB7-Th to efficiently quench all excitons generated in EH-IDTBR, as indicated by the relatively low EH-IDTBR PLQY (52 %, **Fig. S3**). We attributed the suppressed HER rates at < 90 % EH-IDTBR to a core-shell NP morphology as indicated from our structural analyses detailed below. This morphology would allow exciton dissociation at the PTB7-Th/EH-IDTBR heterojunction, but would

subsequently confine most photogenerated electrons to the EH-IDTBR core, preventing efficient electron extraction to the Pt cocatalyst at the NP surface, leading to low photocatalytic activity. Increasing the EH-IDTBR fraction increases the probability of NPs having a partially exposed EH-IDTBR core onto which Pt can be deposited, which improves electron extraction from the NP. This gradually increases the HER rate until the EH-IDTBR mass fraction exceeds a threshold value between 85-90% at which point PTB7-Th can no longer fully encapsulate the EH-IDTBR core; allowing more efficient extraction of both electrons from EH-IDTBR and holes from PTB7-Th, and leading to the maximum HER rate at 90% EH-IDTBR.

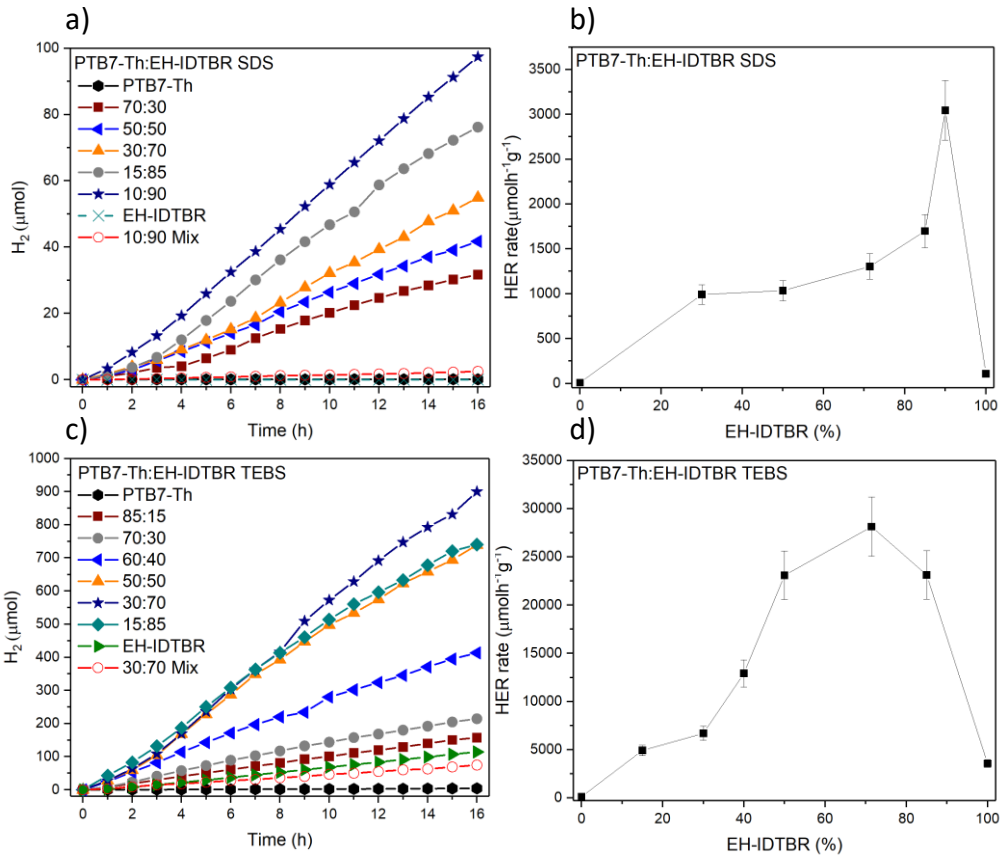

Fig. 2. H_2 evolution vs. time from PTB7-Th/EH-IDTBR nanoparticles formed from a range of PTB7-Th:EH-IDTBR ratios using **a)** SDS **c)** TEBS surfactant. Average H_2 evolution rates of PTB7-Th/EH-IDTBR nanoparticles formed using **b)** SDS **d)** TEBS surfactant over 16 h as a function of blend composition. Conditions: 2 mg PTB7-Th:EH-IDTBR nanoparticles, 0.2 mol/L ascorbic acid (20 mL), pH 2, 5 % (10 µg)

Pt, 300 W Xe lamp (350 to 800 nm), 16 cm^2 reactor. Error bars were calculated as a percentage uncertainty based on 6 repeat measurements.

Core/shell morphologies are common in polymer/small molecule blend nanoparticles prepared from miniemulsions stabilised by SDS.[31–33] This morphology occurs because as the organic solvent is removed, the low volatility components phase segregate to minimize interfacial tension between one another and between the continuous and disperse phases of the emulsion.[34] The chloroform/water interfacial tension in the presence of SDS was twice as high when the chloroform phase contained EH-IDTBR vs. PTB7-Th (**Fig. S4**). Therefore, when forming NPs from a mixed PTB7-Th:EH-IDTBR solution, it is thermodynamically favourable for PTB7-Th to segregate to the surface of the emulsified chloroform droplets in order to minimise their surface tension; eventually forming NPs with a PTB7-Th rich shell and an EH-IDTBR rich core. We attribute the difference in interfacial tensions to a greater affinity between the long aliphatic tail of SDS and the higher alkyl chain density of PTB7-Th compared to EH-IDTBR. Correspondingly, a surfactant with a short aromatic tail, such as sodium 2-(3-thienyl)ethyloxybutylsulfonate (TEBS)[35] was expected to have increased affinity for EH-IDTBR because it can interact more strongly with its exposed aromatic units. In the presence of TEBS, the chloroform/water interfacial tensions were almost identical when the chloroform phase contained EH-IDTBR vs. PTB7-Th (**Fig. S4**). Because the affinity of TEBS for PTB7-Th and EH-IDTBR is approximately equal, radial segregation of PTB7-Th or EH-IDTBR within the NP is no longer thermodynamically favoured. Consequently, when TEBS is employed as the stabilising surfactant, PTB7-Th and EH-IDTBR are expected to be more homogenously mixed throughout the NP and to reside at its surface in approximately equal proportions; providing pathways for efficient extraction of both electrons and holes, thereby increasing the HER rate. Employing TEBS during NP formation dramatically enhanced the HER rates of the blend NPs at all PTB7-Th:EH-IDTBR ratios (**Fig. 2b-c**), with the maximum HER rate (28,133 ± 3067 $\mu molh^{-1}g^{-1}$) increasing by almost an order of magnitude compared to NPs formed using SDS. The optimum blend composition also shifted from an EH-IDTBR mass fraction of 90% to 70%; a composition in which there is more efficient exciton dissociation, as

evidenced by PL quenching (**Fig. S3**), and which has been previously reported to deliver optimal photon conversion efficiency in the active layer of solar cells.[36] An even greater increase in the relative HER rate upon replacing SDS with TEBS as the stabilising surfactant was observed for P3HT:PCBM NPs (**Fig. S5**), which highlights the broad applicability of this technique for optimising the morphology of D/A NP photocatalysts formed from a wide range of solution processable semiconducting polymers and small molecules.

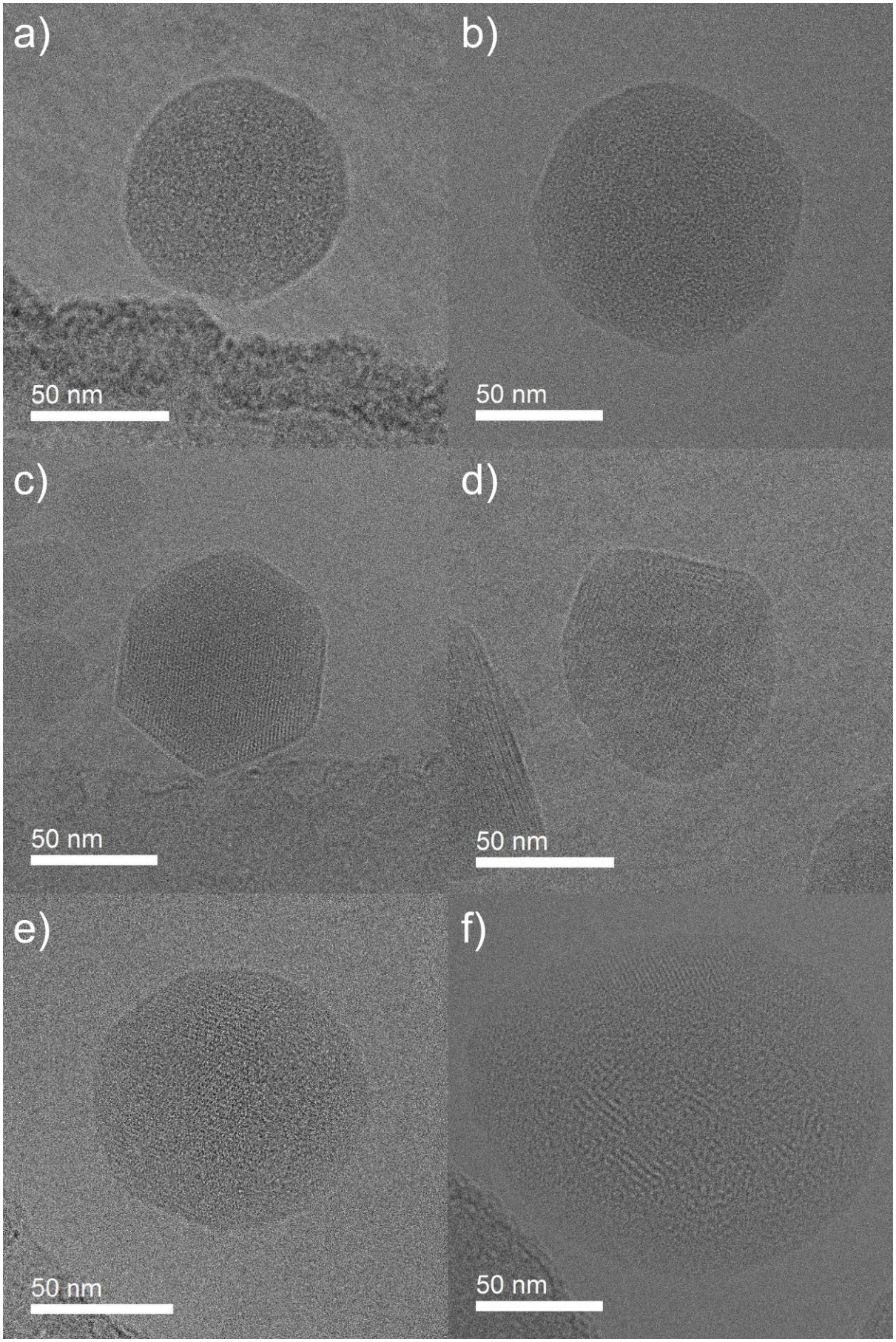
a)
50 nm
b)
50 nm
c)
50 nm
d)
50 nm
e)
50 nm
f)
50 nm

Fig. 3: Bright field cryo-TEM images of nanoparticle photocatalysts showing differences in internal nanoparticle morphology. **a)** PTB7-Th (SDS) **b)** PTB7-Th (TEBS) **c)** EH-IDTBR (SDS) **d)** EH-IDTBR (TEBS) **e)** PTB7-Th:EH-IDTBR 30:70 (SDS) **f)** PTB7-Th/EH-IDTBR 30:70 (TEBS) Note: The dark contrast at the bottom of images **a,c,e** arises from the carbon TEM grid. High resolution images of **a-f** and detailed analysis of images **c-f** can be found in **Fig. S6-12**.

To confirm that the increased HER rates in NPs formed using TEBS were indeed due to a transition from a core-shell to an intermixed NP morphology, the internal morphologies of PTB7-Th:EH-IDTBR NPs fabricated using TEBS and SDS were analysed by cryo-transmission electron microscopy (TEM, **Fig. 3**). This technique was chosen because it can image the NPs in an environment that is close to their native state, and therefore sample preparation is expected to preserve their morphology. Single component PTB7-Th NPs formed using SDS or TEBS (**Fig. 3a-b**) are both amorphous, as indicated by the round NP shape and relatively featureless nanoparticle projection which suggests that there is little structural order in the polymer microstructure. Single component EH-IDTBR NPs formed using SDS and TEBS (**Fig. 3c-d**) both had highly crystalline structures with a lattice spacing of 1.6 nm, clearly visible as lines of alternating high and low electron density. This spacing is consistent with the diffraction peak at 0.39 $Å^{-1}$ in the grazing incidence X-ray diffraction (GIXRD) pattern of an annealed EH-IDTBR thin film.[37] However, EH-IDTBR NPs formed using SDS mostly consisted of a single EH-IDTBR crystal, as indicated by the hexagonal nanoparticle projection and the constant lattice orientation throughout the NP, whereas EH-IDTBR NPs formed using TEBS had a more polycrystalline structure with multiple lattice orientations and visible grain boundaries. The polycrystallinity is attributed to the higher chloroform/water interfacial tension in the presence of TEBS vs. SDS (**Fig. S4**). This induces more rapid EH-IDTBR nucleation and hence a more polycrystalline NP structure. Two component PTB7-Th:EH-IDTBR particles formed using SDS typically exhibit a crystalline phase in the particle core surrounded by a thin amorphous shell. The lattice spacing of the crystalline domain is close to that observed in pure EH-IDTBR (1.7 nm), and the lattice planes have the same orientation throughout the crystalline domain, which suggests that the particle core is

formed from a single EH-IDTBR crystal. In a 95 nm diameter particle shown in **Fig. 3e,** the crystalline core radius is approximately 42 nm, and the amorphous shell radius is approximately 5 nm. Modelling the particle as a sphere, and assuming equal densities of PTB7-Th and EH-IDTBR (**Fig. S7**) shows that the volume of the core and shell domains is consistent with the 30:70 PTB7-Th:EH-IDTBR mass ratio in the blend. Furthermore, the 30:70 PTB7-Th:EH-IDTBR NPs formed using SDS occasionally display an additional periodic spacing in the shell (2.14 nm, **Fig. 5a**) which corresponds to the lamellar stacking distance of PTB7-Th determined by GIXRD.[38] Both these observations strongly suggest that that the NPs formed using SDS are composed of a crystalline EH-IDTBR core surrounded by an amorphous PTB7-Th shell, which is in agreement with the interfacial tensions measured in the presence of SDS (**Fig. S4**) as well as the trend in HER rate vs. blend composition (**Fig. 2a-b**). Two component PTB7-Th:EH-IDTBR NPs formed using TEBS comprise a distributed blend of crystalline and amorphous domains. The crystalline domains showed two different lattice spacings: 1.9 nm and 3.2 nm, both of which correspond to minor peaks in the GIXRD pattern of an EH-IDTBR film at Q = 0.33 $Å^{-1}$ and 0.19 $Å^{-1}$ respectively.[37] This suggests that the rapid crystallisation invoked by TEBS can give rise to multiple EH-IDTBR polymorphs forming within the NP, as has been previously observed in P3HT:EH-IDTBR blend films.[39] Therefore, based on the 30:70 mass ratio of PTB7-Th and EH-IDTBR within the NP, the crystalline regions with 1.9 and 3.2 nm lattice spacings are both assigned to EH-IDTBR. The lack of any apparent radial segregation between the PTB7-Th and EH-IDTBR within the NP, and an approximately equal distribution of PTB7-Th and EH-IDTBR at the NP surface is consistent with the interfacial tensions measured in the presence of TEBS (**Fig. S4**) as well the dramatically increased HER rates achieved with NPs formed using TEBS vs. SDS.

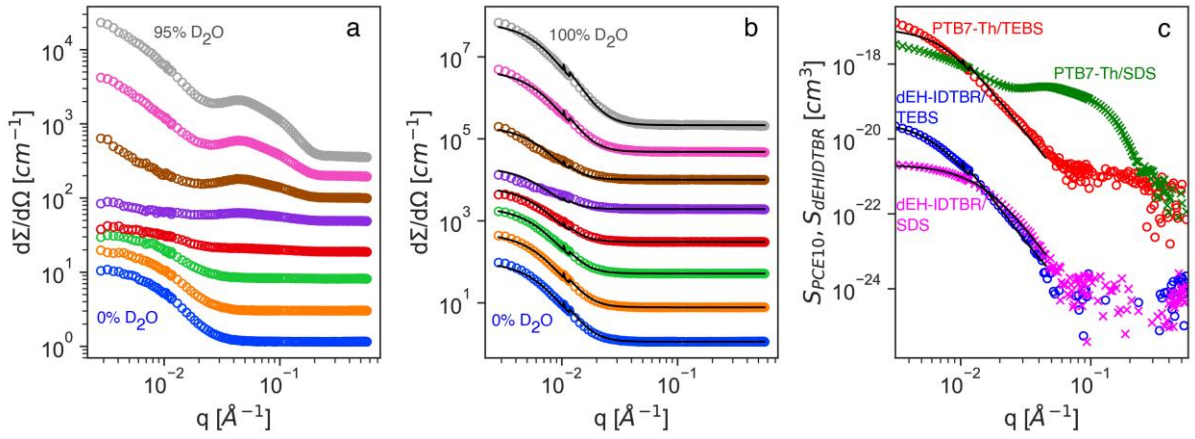

Fig. 4: Small-angle neutron scattering (a, b) and deconstructed partial scattering functions (c) for PTB7-Th (PCE10):dEH-IDTBR nanoparticles in H_2O/D_2O solutions with SDS (a) or TEBS (b) surfactants. In all plots, solid-black lines represent a spherical form-factor model fits to the data. In parts a and b, the curves are successively shifted by $10^{0.5}$and $10^{0.9}$ respectively, while the upper two curves in part c are both shifted by 10^4.

Small-angle neutron scattering (SANS) (**Fig. 4**) of blend NPs of PTB7-Th and deuterated EH-IDTBR (dEH-IDTBR) in D_2O/H_2O solutions further supports the morphological analysis from the cryo-TEM. In **Fig. 4a**, NPs formed using SDS surfactant near the contrast match point of PTB7-Th (volume fraction of 24.7 % D_2O) indicate a spherical dEH-IDTBR core. At contrast conditions near those of dEH-IDTBR (volume fraction of 82.0 % D_2O), a large feature emerges at a middle-q range between $(0.02 < q < 0.2)$ Å^{-1}. Despite the visual appearance of the NPs in **Fig. 3e,** no core-shell model could be fit to the full range of data shown. This includes core-shell models with varying number of shell layers and varying mathematical descriptions of the layer interfaces. To further understand the data, we decomposed the contrast series into partial scattering functions (**Fig. 4c**) which isolate the contributions from the PTB7-Th ($S_{PTB7-Th}(q)$) and dEH-IDTBR ($S_{dEH-IDTBR}(q)$) to the total scattering function, $\frac{d\Sigma}{\Omega}(q)$.[40] This analysis clearly shows that the mid-q feature arises from the PTB7-Th domain while the dEH-IDTBR scattering is described well by a spherical form-factor model. Taken together, these data describe the particle as having a spherical dEH-IDTBR core and a PTB7-Th domain(s) that displays a broad secondary length-scale. Given the cryo-TEM analysis, this secondary

length scale likely still describes a shell-like feature, but there is some additional structural complexity that is not captured in the core-shell models explored here (*e.g.*, local aggregation of PTB7-Th on core-surface, or PTB7-Th/SDS mixed morphologies). The NPs formed using TEBS also showed no significant secondary length scale at any SANS contrast condition (**Fig. 4b).** Simultaneous fits to the spherical form factor model with the radius (R) and log-normal dispersity $\left(\frac{dR}{R}\right)$ parameters constrained across contrast conditions yield reasonable fits ($R = 10.2\ nm, \frac{dR}{R} = 0.57$). The decomposed partial scattering functions (**Fig. 4c**) also show spherical behaviour, with $S_{dEH-IDTBR}(q)$ displaying a better fit than $S_{PTB7-Th}(q)$. The deviations in $S_{PTB7-Th}(q)$ along with those of the full scattering curves at intermediate contrast conditions (**Fig. 4b**) indicate that there is microstructure that is not perfectly described by a spherical model. These observations are likely related to the multiple amorphous and crystalline domains observed in the cryo-TEM (**Fig. 3f**). Overall, the SANS analysis indicates that the blend NPs prepared with TEBS are more intermixed than their SDS counterparts, consistent with the transition from a core-shell NP morphology to a more intermixed D/A heterojunction NP. This is further supported by Kelvin probe force microscopy (KPFM, **Fig. S12**) which shows that the workfunction of the blend NPs formed with TEBS is greater than that of those formed with SDS; suggesting a more EH-IDTBR rich surface in the TEBS-formed NPs.

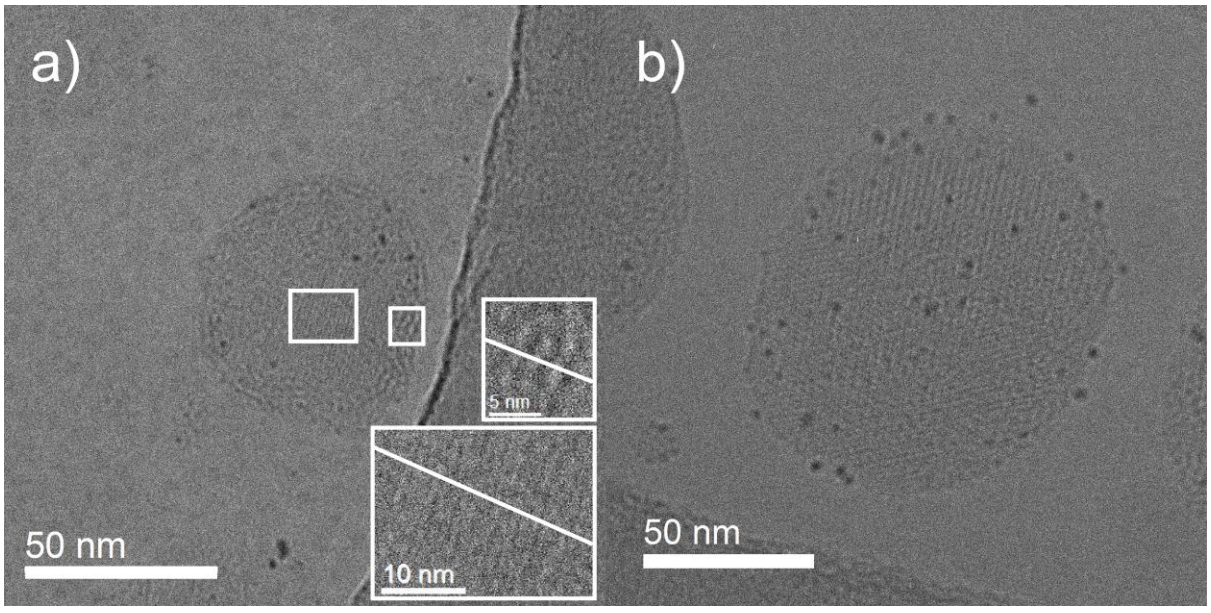

Fig. 5: Cryo TEM images of NPs after deposition of Pt co-catalyst and 20 h H_2 evolution. **a)** PTB7-Th:EH-IDTBR 30:70 (SDS). The upper and lower **insets** are magnified images of the areas in the right and left rectangles respectively. The periodic spacings along the diagonal lines in the upper and lower insets correspond to the lamellar stacking distances of PTB7-Th (2.1 nm) and EH-IDTBR (1.6 nm) respectively (**Fig. S13**).[37,38] **b)** PTB7-Th/EH-IDTBR 30:70 (TEBS).

The photodeposited Pt co-catalyst decorates the surface of the PTB7-Th:EH-IDTBR NPs (**Fig. 5**) and facilitates electron transfer from the photocatalyst to protons in the aqueous phase by providing sites for proton adsorption and electron accumulation.[26,41] Optimising the Pt loading further increased the HER rate of the best performing NPs (30:70 mass ratio PTB7-Th:EH-IDTBR TEBS) to a maximum of 64,426 ± 7022 μmolh-1g-1 at 10% Pt (Fig. S14). To the best of our knowledge, this is by far the highest mass normalized HER rate reported to date for any organic HEP under broadband visible light irradiation.[7,21,42] Measuring the EQEs of the NPs over a range of wavelengths (Fig. 6a) revealed that the NPs were highly active throughout the visible spectrum; achieving EQEs of 2.0%, 2.3%, 4.3%, 5.6% and 6.2% at 400, 500, 620, 660, and 700 nm respectively. This is in contrast to state of the art CNx HEPs which can achieve higher EQEs at wavelengths <450nm but are inactive above 500 nm due to their wide bandgaps.[7] High EQEs at wavelengths >500 nm are essential for the photocatalyst to efficiently utilise photons in the region of maximum solar photon flux, and hence achieve high ηSTH.[8] The EQEs of the PTB7-Th:EH-IDTBR NPs at wavelengths ≥500 nm are significantly higher than those reported for any organic HEP to date,[7,21,42] and make the PTB7-Th:EH-IDTBR HEPs particularly attractive for use in a Z-scheme in conjunction with an efficient wide bandgap OEP such as WO_3[10] or $BiVO_4$[11] that is only active at wavelengths <500 nm.

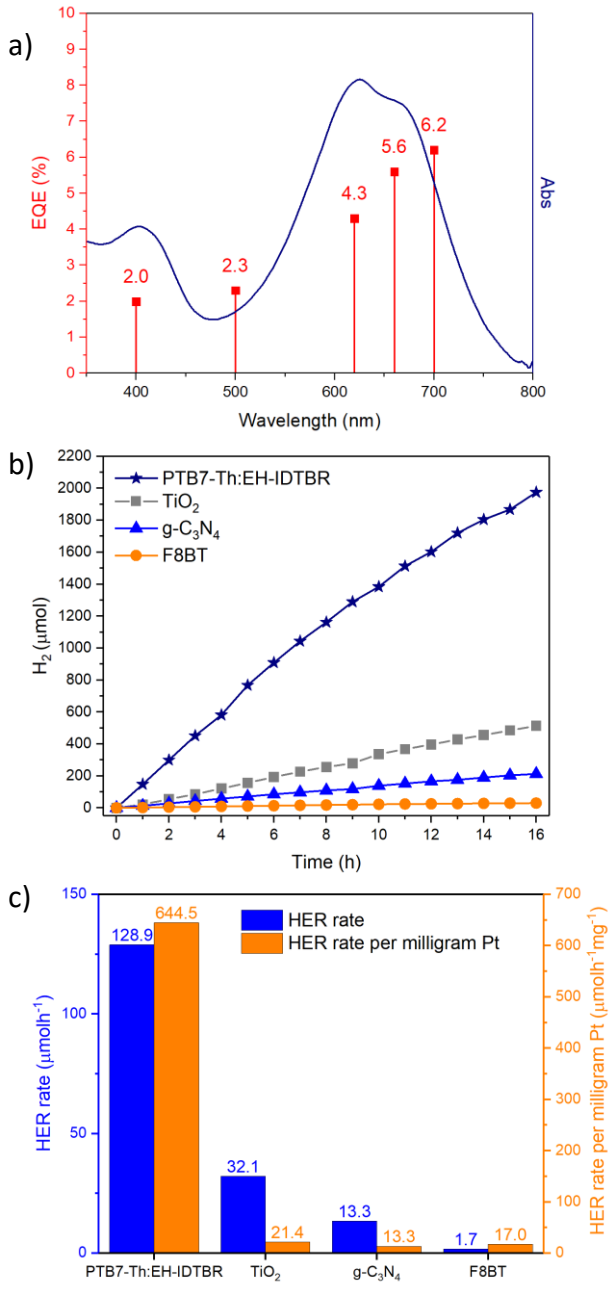

Fig. 6: External quantum efficiencies and performance comparison. **a)** External quantum efficiencies at 400, 500, 620, 660 and 700 ± 10 nm and absorbance spectrum of PTB7-Th:EH-IDTBR 30:70 mass ratio (TEBS) nanoparticle photocatalysts. **b)** H_2 evolution vs. time, **c)** Average H_2 evolution rates of a range of photocatalysts measured over 16 h. **Conditions:** PTB7-Th:EH-IDTBR: 2 mg photocatalyst, 10 % Pt, 20 mL 0.2 mol/L ascorbic acid (AA). P25 TiO_2: 100 mg photocatalyst, 1.5 % Pt, 20 mL 10 % triethanolamine (TEOA). gC3N4**:** 100 mg photocatalyst, 1 % Pt 20 mL 10 % TEOA. F8BT: 2 mg

photocatalyst, 5 % Pt, 20 mL 0.2 mol/L AA. Note: HER rates were higher for TiO_2 and gC_3N_4 with TEOA instead of AA as the sacrificial hole scavenger. Irradiance spectra can be found in **Fig. S15**.

The HER rate of the optimised PTB7-Th:EH-IDTBR NP photocatalysts was compared to a range of benchmark materials measured in the same reactor, under illumination from the same light source (**Fig. 6b-c**). To ensure a fair comparison between photocatalysts, the HER rates were measured under saturated conditions (0 % light transmission through the reactor throughout the photocatalyst's absorption range).[43] The Pt loadings of g-C_3N_4 (1 %)[44] TiO_2 (1.5 %)[45] and F8BT (5 %)[26] were chosen based on previously reported optima, and the photocatalytic activities reported for g-C_3N_4 and TiO_2 are the higher of two measurements taken in the presence of different sacrificial reagents (ascorbic acid or triethanolamine). HER rates were compared in terms of the absolute amount of H_2 produced per hour.[46] The average HER rate over 16h of the PTB7-Th:EH-IDTBR NP photocatalysts (128.9 $\mu molh^{-1}$) was over 4 times higher than that of TiO_2 (32.1 $\mu molh^{-1}$), almost 10 times higher than that of commercial g-C_3N_4 (13.3 $\mu molh^{-1}$), and over 75 times higher than poly(9,9-dioctylfluorene-alt-benzothiadiazole) (F8BT) NPs (1.7 $\mu molh^{-1}$), a commonly studied single component conjugated polymer photocatalyst.[26,47] Although the optimum Pt loading (10 %) was significantly higher for the PTB7-Th:EH-IDTBR NPs than for the other photocatalysts, when comparing photocatalytic activities in terms of HER rate per total mass of Pt used (**Fig. 6d**) the activity of the PTB7-Th:EH-IDTBR NPs rises even further above the g-C_3N_4 and TiO_2 benchmarks. This is because the strong light absorption and efficient charge generation of the PTB7-Th:EH-IDTBR NPs allows them to produce significantly more photogenerated charges per unit mass of photocatalyst. This increases the turnover frequency of the Pt co-catalyst (**Table S3**) compared to the benchmark photocatalysts, which is highly advantageous in terms of both cost and scalability.[48]

We have demonstrated the fabrication of organic NP HEPs with an internal D/A semiconductor heterojunction, which significantly improves charge generation inside the NP bulk, and thus greatly enhances photocatalytic activity compared to NPs formed from a single organic semiconductor. By varying the stabilizing surfactant employed during NP fabrication, it was possible to optimize the heterojunction morphology from an unfavourable core-shell structure to a more intimately mixed blend. This improved charge extraction from the NPs and increased the HER rate of PTB7-Th:EH-IDTBR NPs by almost an order of magnitude, leading to the unprecedentedly high HER rate of 64,426 ± 7022 $\mu molh^{-1}g^{-1}$ under broadband visible light illumination, photocatalytic activity throughout the visible spectrum, and EQEs exceeding 5% at 660 to 700 nm. The EQEs at wavelengths >500 nm are the highest reported for any organic HEP to date, and may provide a pathway to increased ηSTH of current Z-schemes via improved visible light utilization. Furthermore, the NP fabrication and heterojunction optimization process provides a platform for the vast library of existing soluble organic semiconductors to be processed into NP photocatalysts energetically tailored to drive a wide range of redox chemistries including OWS, CO_2 reduction,[49] and N_2 fixation,[50] which all rely on the same fundamental photon-to-electron conversion processes as photocatalytic hydrogen evolution.

References

1. Hoffert, M. I. *et al.* Advanced technology paths to global climate stability: energy for a greenhouse planet. *Science* **298**, 981–7 (2002).

2. Creutzig, F. *et al.* The underestimated potential of solar energy to mitigate climate change. *Nat. Energy* **2**, 17140 (2017).

3. Pinaud, B. A. *et al.* Technical and economic feasibility of centralized facilities for solar hydrogen production via photocatalysis and photoelectrochemistry. *Energy Environ. Sci.* **6**, 1983 (2013).

4. FUJISHIMA, A. & HONDA, K. Electrochemical Photolysis of Water at a Semiconductor Electrode. *Nature* **238**, 37–38 (1972).

5. Goto, Y. *et al.* A Particulate Photocatalyst Water-Splitting Panel for Large-Scale Solar Hydrogen Generation. *Joule* **2**, 509–520 (2018).

6. Wang, X. *et al.* A metal-free polymeric photocatalyst for hydrogen production from water under visible light. *Nat. Mater.* **8**, 76–80 (2009).

7. Zhang, G. *et al.* Ionothermal Synthesis of Triazine-Heptazine-Based Copolymers with Apparent Quantum Yields of 60 % at 420 nm for Solar Hydrogen Production from “Sea Water”. *Angew. Chemie Int. Ed.* **57**, 9372–9376 (2018).

8. Maeda, K. & Domen, K. Photocatalytic Water Splitting: Recent Progress and Future Challenges. *J. Phys. Chem. Lett.* **1**, 2655–2661 (2010).

9. Wang, Y. *et al.* Mimicking Natural Photosynthesis: Solar to Renewable H_2 Fuel Synthesis by Z-Scheme Water Splitting Systems. *Chem. Rev.* **118**, 5201–5241 (2018).

10. Bamwenda, G. R. & Arakawa, H. The visible light induced photocatalytic activity of tungsten trioxide powders. *Appl. Catal. A Gen.* **210**, 181–191 (2001).

11. Zhu, M., Sun, Z., Fujitsuka, M. & Majima, T. Z-Scheme Photocatalytic Water Splitting on a 2D

Heterostructure of Black Phosphorus/Bismuth Vanadate Using Visible Light. *Angew. Chemie Int. Ed.* **57**, 2160–2164 (2018).

12. Kim, J. H. & Lee, J. S. Elaborately Modified $BiVO_4$ Photoanodes for Solar Water Splitting. *Adv. Mater.* **31**, 1806938 (2019).

13. Zhang, P., Zhang, J. & Gong, J. Tantalum-based semiconductors for solar water splitting. *Chem. Soc. Rev.* **43**, 4395–4422 (2014).

14. Yuan, Y.-J., Chen, D., Yu, Z.-T. & Zou, Z.-G. Cadmium sulfide-based nanomaterials for photocatalytic hydrogen production. *J. Mater. Chem. A* **6**, 11606–11630 (2018).

15. Zhu, X. *et al.* Black Phosphorus Revisited: A Missing Metal-Free Elemental Photocatalyst for Visible Light Hydrogen Evolution. *Adv. Mater.* **29**, 1605776 (2017).

16. Sachs, M. *et al.* Understanding structure-activity relationships in linear polymer photocatalysts for hydrogen evolution. *Nat. Commun.* **9**, 4968 (2018).

17. Zhang, X. *et al.* Biomass Nanomicelles Assist Conjugated Polymers/Pt Cocatalysts To Achieve High Photocatalytic Hydrogen Evolution. *ACS Sustain. Chem. Eng.* **7**, 4128–4135 (2019).

18. Banerjee, T. & Lotsch, B. V. The wetter the better. *Nat. Chem.* **10**, 1175–1177 (2018).

19. Mikhnenko, O. V., Blom, P. W. M. & Nguyen, T.-Q. Exciton diffusion in organic semiconductors. *Energy Environ. Sci.* **8**, 1867–1888 (2015).

20. Sun, C. *et al.* Interface design for high-efficiency non-fullerene polymer solar cells. *Energy Environ. Sci.* **10**, 1784–1791 (2017).

21. Wang, X. *et al.* Sulfone-containing covalent organic frameworks for photocatalytic hydrogen evolution from water. *Nat. Chem.* **10**, 1180–1189 (2018).

22. Takanabe, K. *et al.* Photocatalytic hydrogen evolution on dye-sensitized mesoporous carbon nitride photocatalyst with magnesium phthalocyanine. *Phys. Chem. Chem. Phys.* **12**, 13020 (2010).

23. Low, J., Yu, J., Jaroniec, M., Wageh, S. & Al-Ghamdi, A. A. Heterojunction Photocatalysts. *Adv. Mater.* **29**, 1601694 (2017).

24. Richards, J. J., Whittle, C. L., Shao, G. & Pozzo, L. D. Correlating Structure and Photocurrent for Composite Semiconducting Nanoparticles with Contrast Variation Small-Angle Neutron Scattering and Photoconductive Atomic Force Microscopy. *ACS Nano* **8**, 4313–4324 (2014).

25. Wang, L. *et al.* Organic Polymer Dots as Photocatalysts for Visible Light-Driven Hydrogen Generation. *Angew. Chemie Int. Ed.* **55**, 12306–12310 (2016).

26. Kosco, J. *et al.* The Effect of Residual Palladium Catalyst Contamination on the Photocatalytic Hydrogen Evolution Activity of Conjugated Polymers. *Adv. Energy Mater.* 1802181 (2018). doi:10.1002/aenm.201802181

27. Liu, A., Tai, C.-W., Holá, K. & Tian, H. Hollow polymer dots: nature-mimicking architecture for efficient photocatalytic hydrogen evolution reaction. *J. Mater. Chem. A* **7**, 4797–4803 (2019).

28. Trasatti, S. The absolute electrode potential: an explanatory note (Recommendations 1986). *J. Electroanal. Chem. Interfacial Electrochem.* **209**, 417–428 (1986).

29. Staff, R. H., Landfester, K. & Crespy, D. Recent Advances in the Emulsion Solvent Evaporation Technique for the Preparation of Nanoparticles and Nanocapsules. in 329–344 (Springer, Cham, 2013). doi:10.1007/12_2013_233

30. Cha, H. *et al.* Suppression of Recombination Losses in Polymer:Nonfullerene Acceptor Organic Solar Cells due to Aggregation Dependence of Acceptor Electron Affinity. *Adv. Energy Mater.* **9**, 1901254 (2019).

31. Schwarz, K. N., Farley, S. B., Smith, T. A. & Ghiggino, K. P. Charge generation and morphology in P3HT : PCBM nanoparticles prepared by mini-emulsion and reprecipitation methods. *Nanoscale* **7**, 19899–19904 (2015).

32. Ulum, S. *et al.* Determining the structural motif of P3HT:PCBM nanoparticulate organic

photovoltaic devices. *Sol. Energy Mater. Sol. Cells* **110**, 43–48 (2013).

33. Holmes, N. P. *et al.* Nano-domain behaviour in P3HT:PCBM nanoparticles, relating material properties to morphological changes. *Sol. Energy Mater. Sol. Cells* **117**, 437–445 (2013).

34. Ge, X. *et al.* Four reversible and reconfigurable structures for three-phase emulsions: extended morphologies and applications. *Sci. Rep.* **7**, 42738 (2017).

35. Subianto, S. *et al.* Sulfonated Thiophene Derivative Stabilized Aqueous Poly(3-hexylthiophene):Phenyl-C_{61}-butyric Acid Methyl Ester Nanoparticle Dispersion for Organic Solar Cell Applications. *ACS Appl. Mater. Interfaces* **10**, 44116–44125 (2018).

36. Baran, D. *et al.* Robust nonfullerene solar cells approaching unity external quantum efficiency enabled by suppression of geminate recombination. *Nat. Commun.* **9**, 2059 (2018).

37. Holliday, S. Extended Linear Acceptors with an Indacenodithiophene Core. in 63–85 (Springer, Cham, 2018). doi:10.1007/978-3-319-77091-8_4

38. Huang, L. *et al.* Vertical Stratification Engineering for Organic Bulk-Heterojunction Devices. *ACS Nano* **12**, 4440–4452 (2018).

39. Holliday, S. *et al.* High-efficiency and air-stable P3HT-based polymer solar cells with a new non-fullerene acceptor. *Nat. Commun.* **7**, 11585 (2016).

40. Endo, H., Schwahn, D. & Cölfen, H. On the role of block copolymer additives for calcium carbonate crystallization: Small angle neutron scattering investigation by applying contrast variation. *J. Chem. Phys.* **120**, 9410–9423 (2004).

41. McKone, J. R., Marinescu, S. C., Brunschwig, B. S., Winkler, J. R. & Gray, H. B. Earth-abundant hydrogen evolution electrocatalysts. *Chem. Sci.* **5**, 865–878 (2014).

42. Stegbauer, L., Schwinghammer, K. & Lotsch, B. V. A hydrazone-based covalent organic framework for photocatalytic hydrogen production. *Chem. Sci.* **5**, 2789–2793 (2014).

43. Qureshi, M. & Takanabe, K. Insights on Measuring and Reporting Heterogeneous

Photocatalysis: Efficiency Definitions and Setup Examples. *Chem. Mater.* **29**, 158–167 (2017).

44. Maeda, K. *et al.* Photocatalytic Activities of Graphitic Carbon Nitride Powder for Water Reduction and Oxidation under Visible Light. *J. Phys. Chem. C* **113**, 4940–4947 (2009).

45. Haselmann, G. M. & Eder, D. Early-Stage Deactivation of Platinum-Loaded TiO_2 Using In Situ Photodeposition during Photocatalytic Hydrogen Evolution. *ACS Catal.* **7**, 4668–4675 (2017).

46. Zhang, G., Lan, Z.-A. & Wang, X. Conjugated Polymers: Catalysts for Photocatalytic Hydrogen Evolution. *Angew. Chemie Int. Ed.* **55**, 15712–15727 (2016).

47. Pati, P. B. *et al.* An experimental and theoretical study of an efficient polymer nano-photocatalyst for hydrogen evolution. *Energy Environ. Sci.* **10**, 1372–1376 (2017).

48. Zou, X. & Zhang, Y. Noble metal-free hydrogen evolution catalysts for water splitting. *Chem. Soc. Rev.* **44**, 5148–5180 (2015).

49. Yu, J., Low, J., Xiao, W., Zhou, P. & Jaroniec, M. Enhanced Photocatalytic CO_2 -Reduction Activity of Anatase TiO_2 by Coexposed {001} and {101} Facets. *J. Am. Chem. Soc.* **136**, 8839–8842 (2014).

50. Li, H., Shang, J., Ai, Z. & Zhang, L. Efficient Visible Light Nitrogen Fixation with BiOBr Nanosheets of Oxygen Vacancies on the Exposed {001} Facets. *J. Am. Chem. Soc.* **137**, 6393–6399 (2015).

Methods

Nanoparticle fabrication:

Individual stock solutions (0.50 mg/mL) of PTB7-TH and EH-IDTBR were prepared in chloroform. The solutions were heated overnight (80 °C) to ensure complete dissolution and filtered (0.2 um PTFE). Nanoparticle precursor solutions were prepared from the stock solutions by mixing them in the ratio of the desired nanoparticle composition. 5 mL of the nanoparticle precursor solution was then added to a 0.5 wt.% solution of surfactant (SDS or TEBS) in water (10 mL), and stirred vigorously for 15 min at 40 °C to form a pre-emulsion, which was then sonicated for 5 min with an ultrasonic processor (Sonics VibraCell VCX130PB) to form a mini-emulsion. The mini-emulsion was heated at 85 °C under a stream of air to remove the chloroform, leaving a surfactant stabilised nanoparticle dispersion in water. Finally, the dispersion was filtered (0.45 µm glass fibre) to remove any large aggregates or debris from the processor tip.

DLS:

The size distribution of each nanoparticle batch was measured by dynamic light scattering (DLS, Malvern Zetasizer ZS, **Fig. S1**, **Table S1**). **Fig. S1** shows that all NP batches had unimodal size distributions and that the Z_{avg} hydrodynamic diameter between batches remained relatively constant at 50-80 nm regardless of whether SDS or TEBS was used as the stabilising surfactant. TEBS narrowed the NP size distributions and slightly increased the Z_{avg} NP size for all PTB7-TH:EH-IDTBR ratios, but overall all NP batches were of a similar size. This is important when comparing HER rates between batches, because NP size affects the total available surface area, which would likely affect the HER rate. Having samples with similar size distributions minimises this variation and allows the effects of nanoparticle composition and morphology to be isolated.

TEM:

Cryo Transmission Electron Microscopy (cryoTEM) of the samples was carried out with a Titan Krios 80-300 TEM from Thermo-Fisher Scientific, USA. This microscope is optimized for carrying out

cryoTEM analysis of liquid samples. It is also equipped with an energy-filter of model GIF Quantum 968 from Gatan, Inc., USA, underneath the column to filter the energy-loss electrons to improve the contrast in the acquired images. Moreover, behind the GIF column, a highly sensitive direct electron complementary metal oxide semiconductor (CMOS) camera of model K2, also from Gatan, Inc., USA, was installed for the recording of high-resolution images at extremely low electron dose conditions (~1 e/Å2). Specimen preparation of samples for cryoTEM analysis was carried out by using an automated plunge-freezing tool of model Vitrobot Mark-IV. Moreover, the specimens were prepared with a special type of copper TEM-grid of model Quatifoil MultiA. These grids have a carbon layer with various size holes and were chosen with a purpose of varying ice-thickness in the holes. In this way, the chance of organic particles being present in the specimen was dramatically higher than with the single hole-size carbon containing grid. Each specimen was prepared by placing 3.5 micro-litre of solution onto grids followed by 1 second of blotting-time and plunge-freezing into liquid ethane cryogen. The cryoTEM analysis was performed by setting the microscope at the accelerating voltage of 300 kV. Prior to the analysis, the microscope as well as GIF were aligned to have higher quality images. Furthermore, the images were recorded under so called dose-fractionation conditions. In fact, instead of acquiring a single frame with total electron beam exposure time, the images were acquired in stacks that contained frames whose exposure time was more than ten times smaller than the total exposure time. The acquired stacks were then aligned and summed along z-direction in order to have final images. This exercise of image-recording ensured higher quality images of organic particles with as minimum damage as possible. The total electron dose given to images, acquired at low-magnifications (<50,000X) was kept below 10 e/Å^2. Whereas, higher magnification images (>100,000X) received the electron dose of about 20 e/Å^2 so as to maintain a good signal-to-noise condition. It is to be noted that the entire image acquisition as well as processing was performed using Gatan Microscopy Suite of version 3.2.

Hydrogen evolution:

Hydrogen evolution from PTB7-TH/EH-IDTBR nanoparticles was measured using ascorbic acid (AA) as a sacrificial electron donor. PTB7-TH/EH-IDTBR nanoparticles with varying PTB7-TH:EH-IDTBR ratios (2 mg) in 0.2 M AA (20 mL) were loaded into a recirculating batch reactor (area = 452 mm^2) which has been previously reported.[43] The desired Pt loading was achieved by adding a specific amount of aqueous potassium hexachloroplatinate solution (0.401 mg/mL Pt). The reactor was evacuated and purged with Ar 5 times to remove oxygen, and the pressure was set to 100 Torr. The suspension was stirred and illuminated with a 300 W Xe lamp (Asahi Max 303) fitted with a UV-vis mirror module (350-800 nm) and H_2 evolution was quantified by a gas chromatograph equipped with a thermal conductivity detector. The same method was used to measure H_2 evolution from TiO_2 and g-C_3N_4, except in this case 100 mg of photocatalyst was used, and the reaction was carried out either in 0.2 M AA, or 10 vol.% triethanolamine.

EQE measurements:

EQE measurements were carried out in the same way as hydrogen evolution measurements, but with suitable band pass filters fitted to the light source. The sample was first illuminated under unfiltered light (350-800 nm) for 4 h to complete Pt photodeposition. Then the reactor was evacuated and purged with Ar 5 times to remove all of the H_2 evolved during this time. The light source was fitted with a band pass filter, and illuminated with filtered light within a narrow wavelength range (irradiance spectra in **Fig. S16**). The EQE was calculated using **Equation 1**, where nH_2 represents the number of moles of H_2 evolved per hour, and n photons represents the total number of photons incident on the reactor per hour. Photon flux was measured using a calibrated spectrometer (Ocean Optics USB2000 calibrated with an Ocean Optics DH3-plus light source) fitted with a fibre optic cable and a 0.4778 cm^2 cosine corrector.

Equation 1:

$$EQE\ (\%) = \frac{200n\ H_2}{n\ photons}$$

Atomic Force Microscopy:

Nanoparticles were drop-cast on ITO coated glass substrates and characterised with a SOLVER NEXT SPM (NT-MDT) using an atomic force microscopy (AFM) measuring head. To confirm the core-shell morphology, samples were placed in a plasma-asher (HPT-100, Henniker plasma) for two ten second periods, a few nanometres of material was removed from the surface of the nanoparticles. Topography and surface potential were measured in semi-contact mode using a 20 nm PtIr-coated conductive 0.01-0.025 Ohm-cm Antimony (n) doped Si cantilever (SCM-PIT, Veeco). The cantilever had a resonant frequency and stiffness of 60-100 kHz and 1-5 N/m, respectively. The work-function of the tip was estimated by measuring the contact potential difference (V_{CPD}) of a gold standard (5.1 eV) from Digital Instruments Veeco Metrology Group and using the equation:

Equation 2

$$V_{CPD} = \frac{\Phi_{tip} - \Phi_{sample}}{-e}$$

Where ϕ is the work-function and e the charge of an electron. The work-function of the tip was found to be 5.05 eV (mean V_{CPD} for gold = 50 mV from **Fig. S12e**). To confirm, a commercial ITO sample was measured (**Fig. S12f**) and the work-function estimated as 4.84 eV (mean V_{CPD} for ITO = -213 mV).

Surface and interfacial tension measurements:

Surface and interfacial tensions were measured with a Kruss Tensiometer using the ring method. The probe was rinsed in water and heated until it was red hot. The glass vessel used to hold the liquid was cleaned with acetone and rinsed with water. To confirm no contamination, before each measurement, the surface tension of water was measured. The liquid to be measured was placed in the glass vessel, and the temperature allowed to equilibrate for 30 min. The concentration of TEBS or SDS in deionized water was 0.5 wt % and for PTB7-TH or EH-IDTBR 0.5 mg/ml in chloroform. The surface tension

measurements were performed by attaching the probe to the balance. The glass vessel containing the liquid to be measured was raised until the probe was just above the liquid. The probe and liquid were slowly brought together until in contact with one another.

Where F is the force acting on the balance. The contact angle can be assumed to be zero as the plate is roughened platinum and optimally wetted. The plate method can be used for interfacial tension, but the light phase should have a lower surface tension than the heavy phase. Which is not the case (**Fig. S4 and S5**). We therefore use the ring method. An advantage of the ring method is the wetted length is greater than the plate method. Which leads to a greater force on the balance and more accurate results. This effect is not relevant for surface tension, only interfacial tension, but for comparison we have performed surface tension measurements (**Fig. S5**). After contact with the liquid, the sample is lowered until a maximum force (F_{max}) on the ring is recorded. The interfacial tension was calculated according to equation 3.

Equation 3

$$\sigma = \frac{F_{max} - F_v}{L \cdot cos\theta}$$

Where F_v is the weight of liquid volume, L the wetted length, and Θ the contact angle. Θ = 0 because the force vector is parallel to the direction of motion. A Harkins and Jordan correction factor is applied to correct for the curvature of the film being greater on the inside than the outside of the ring. The results of the interfacial tension measurements are shown in **Fig. S4**.

Data availability

The data shown in the plots and that support the findings of this study are available from the corresponding authors on reasonable request.

Acknowledgements

The research reported in this publication was supported by funding from King Abdullah University of

Science and Technology (KAUST) Office of Sponsored Research (OSR) under Award No: OSR-2018-CARF/CCF-3079 and OSR-2015-CRG4-2572. This work was supported by the nSoft consortium.

Author information

These authors contributed equally: Jan Kosco, Matthew Bidwell

Ethics Declarations

The authors declare no competing interests.

Additional information

Certain commercial products or company names are identified here to describe our study adequately. Such identification is not intended to imply recommendation or endorsement by the National Institute of Standards and Technology, nor is it intended to imply that the products or names identified are necessarily the best available for the purpose.